Influence of fabrication processes on transport properties of superconducting niobium nitride nanowires

Manju Singh[1,2], Rishu Chaujar[3], Sudhir Husale[1,2], S. Grover[4], Amit P. Shah[4], Mandar M. Deshmukh[4], Anurag Gupta[1,2], V. N. Singh[1,2], V. N. Ojha[1,2], D. K. Aswal[1,2] and R. K. Rakshit[1,2,*]

[1]Academy of Scientific and Innovative Research, CSIR-NPL Campus, Dr K.S. Krishnan Marg, New Delhi 110 012, India
[2]National Physical Laboratory, Council of Scientific and Industrial Research, Dr K.S. Krishnan Marg, New Delhi 110 012, India
[3]Microelectronics Research Laboratory, Department of Engineering Physics, Delhi Technological University, Bawana Road, Delhi 110 042, India
[4]Department of Condensed Matter Physics and Materials Science, Tata Institute of Fundamental Research, Homi Bhabha Road, Mumbai 400 005, India

Fabrication of niobium nitride (NbN) superconducting nanowires based on focused ion beam (FIB) milling and electron beam lithography (EBL) is presented. The NbN films were deposited using reactive magnetron sputtering. Argon-to-nitrogen ratio turned out to be a crucial factor in synthesizing high quality superconducting NbN. Critical temperatures (T_c) of around 15.5 K were measured for films with a thickness of around 10 nm. Zero-field-cooled magnetization was measured to optimize the superconducting properties of ultra thin NbN films. The transport behaviour was studied using conventional resistance vs temperature and current-voltage characteristics down to 2 K. Effect of gallium contamination on superconducting properties has been discussed. Whereas the various processing steps of standard EBL route do not have any significant impact on the superconducting transition temperature as well as on the transition width of nanowires, there is significant degradation of superconducting properties of nanowires prepared using FIB. This has been attributed to gallium ion implantation across the superconducting channel. Although the effect of gallium implantation may have technological limitations in designing fascinating single photon detector architectures, it provides some interesting low-dimensional superconducting properties.

Keywords: DC magnetron sputtering, EBL, FIB, niobium nitride, superconducting nanostructure, thin films.

ALTHOUGH research initiatives towards single photon detection are not new, the demand for detector performance that goes beyond the performance of conventional single photon detectors has increased significantly over the past years, and is expected to grow due to current interest in the emerging field of quantum information processing[1–17].

In the light of recent developments in the field of quantum information technologies, it is absolutely essential to redefine candela, the SI unit of luminous intensity in terms of number of photons as well. Quantum metrology towards photon-based standards for optical radiation demands exploring newer and better single photon detection system[18]. Photomultiplier tubes (PMT) and solid state single-photon avalanche photodiodes (SPAD) are widely being used for detection of a single photon in many applications in the visible wavelength range due to their reasonable performance matrices and also due to their ambient/moderate operating temperatures. Between these two, SPAD is better in many ways due to its better detection efficiency (η), low dark count rate (DCR) and low time jitter (Δt). The figure of merit ($\eta/(D\Delta t)$) for InGaAs-SPAD is four orders of magnitude better than that of PMT at 1550 nm wavelength[3]. However, the major drawback of both these detectors in contemporary photon-counting technologies such as, quantum key distribution (QKD) and quantum computation which exploit tele-communication wavelengths (1310 and 1550 nm) is that their device performance deteriorates significantly in near infrared wavelength range. Relatively new classes of detectors based on superconductors hold promise over conventional semiconductor detector technologies due to their single photon counting capability spanning from the visible to infrared range. The superconducting transition edge sensors (TES) offer very high detection efficiency (more than 90%) and almost negligible dark counts[19]. However their slow response (100s of kHz count rate) and milli Kelvin (mK) operating temperature raise questions on their successful implementation in quantum information and quantum optical experiments. On the other hand, despite low detection efficiency in general, due to low DCR and picoseconds time jitter the superconducting nanowires single photon detectors (SNSPDs) are better or comparable to the best TES. Moreover, due to its GHz clock rate and relatively high operating temperature (few

Kelvin) SNSPD has been successfully used in the demonstration of quantum communications[3,7,8].

The most commonly used material for SNSPDs is niobium nitride (NbN) because of its higher superconducting transition temperature (T_c) compared to conventional superconductors, and stability over repeated thermal cycling. Exceptional mechanical properties such as hardness and high wear resistance also help in preserving its superconducting properties after several lithographic steps. Also, because NbN is a highly refractory material which enhances optical absorption, over the years it has become chosen superconductor to understand the fundamentals and to explore the technological aspects of superconducting nanostructure-based single photon detectors.

Several nanofabrication techniques such as EBL[20–21], ion irradiation[22], local oxidation using an atomic force microscope[23], and milling FIB[24–27] have been employed to create junctions or patterned structures. Every route has its own pros and cons. For instance, although FIB milling is an extraordinarily flexible and straightforward approach for nano patterning, it needs to overcome the issue of gallium contamination[28–30]. Nevertheless, Zhang et al.[26] were successful in fabricating high quality superconducting nanowires from ultrathin MgB_2 films using FIB milling technique. Bachar et al.[27] demonstrated FIB-based design of SNSPD on the core of a single mode optical fibre. Protective layers such as aluminium or gold can be used to prevent degradation due to gallium irradiation during FIB milling which can later be etched out once the desired patterns are made.

Our work presented in this article deals with fabrication of ultrathin NbN films with desired superconducting properties, and fabrication of superconducting nanostructures for single photon detectors. Thin films of NbN have been deposited using reactive magnetron sputtering. The dependence of T_c as a function of argon (Ar) and nitrogen (N_2) has been studied systematically. Relatively thick (50 nm) NbN and single crystal MgO (001) as substrate were preferred for optimization of initial deposition parameters to facilitate epitaxial growth. In the next step, ultrathin films of NbN on 300 nm SiO_2 coated silicon (Si) substrates at a lower temperature were optimized to avoid primarily the formation of stable Nb_2O_5 dielectric which crystallizes at around 500°C (ref. 31) and, secondly the degradation of underlying layers or pre-coated polymer resist. Although thicker films were grown at relatively low temperature and even at ambient substrate temperature, synthesizing ultrathin NbN films with desired superconducting properties has always been a challenge due to proximity effect[32–34]. In this study, we have used FIB milling and EBL-based routes for nano patterning of thin NbN films. Although the superconducting property is largely suppressed by gallium ion implantation, a moderate T_c of about 6 K clearly shows the potential of FIB milling technique for patterning superconducting films.

Magnetization measurements were carried out using a Quantum Design (USA make) 7T magnetic property measurement system (MPMS). The conventional four-point probe method was used to evaluate superconducting properties of the films in a customized, variable temperature, liquid nitrogen shielded, liquid helium cryostat down to 1.8 K (Cryo Industries of America Inc.).

Results and discussion

NbN with resistivity ranging between 1 and 10 Ωcm films was deposited on MgO (100) single crystal as well as on 300 nm SiO_2 coated p-type boron doped Si(100) substrates by reactive dc magnetron sputtering of a 2 inch diameter 99.95% pure metallic Nb target in a reactive gas mixture of 6N pure Ar and N_2. The flow rates of Ar and N_2 were controlled and monitored separately to understand their role on T_c. Initially the sputtering chamber was pumped down to achieve a base vacuum corresponding to 1×10^{-7} mbar of chamber pressure. The deposition was carried out at a total chamber pressure of 7×10^{-3} mbar. The MgO substrates were kept at 600°C during deposition, whereas thinner films of NbN were deposited at 200°C on Si/SiO_2. MgO and Si/SiO_2 substrates were prebaked in base vacuum at 800°C and 200°C respectively, for an hour prior to deposition. Thickness of the deposited films was measured using a stylus profiler. The deposition rate was estimated to be 20 nm/min. Once optimized, the process parameters were kept unchanged and thinner films were grown on Si/SiO_2 at the same deposition rate. Figure 1 shows the dependence of T_c on the ratio of Ar and N_2 gas mixture. T_c has been deduced from
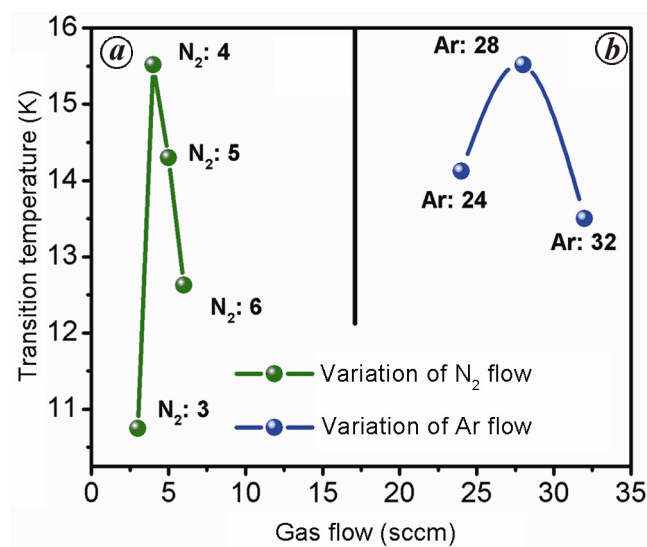
Figure 1. Dependence of superconducting transition temperature (T_c) of NbN thin films on the ratio of Ar/N_2 gas mixture. Plot *a* is for the films synthesized by keeping the Ar flow fixed at 28 sccm while the N_2 flow was varied from 3 to 6 sccm. *b* shows the variation of T_c with argon flow for films synthesized at a fixed 4 sccm N_2 flow.

zero-field-cooled (ZFC) magnetization measurements as a function of temperature. The left panel is a plot of variation of T_c with N_2 at constant 28 sccm Ar flow. T_c initially increased with increase in N_2 content, reached a maximum at 4 sccm of N_2 flow and decreased with further increase in N_2 flow. Dependence of T_c follows a similar trend (right panel) when the Ar content in the chamber during deposition was varied from 24 sccm to 32 sccm for a fixed N_2 flow (4 sccm). The T_c went through a maximum at 28 sccm Ar flow. Similar trends were observed in previous studies and this has been attributed to gradual change in crystal structures[35]. The maximum T_c of NbN thin films is associated with the cubic B1 (fcc NaCl) phase. The monotonic decrease of T_c from its maximum value on both sides (Figure 1 *a, b*) with the change in ratio of Ar and N_2 mixture from the optimum value is associated with the deviation of metal to nitrogen ratio from unity, leading to a gradual transition from cubic to tetragonal phase. Earlier Hall effect measurements on NbN thin films revealed that the carrier concentration of NbN is sensitive to deposition and that the T_c of NbN is governed primarily by the carrier density. The deviation from equiatomic stoichiometric NbN leads to reduction in carrier density due to increase in either Nb or N vacancies. It is possible that the structural transition is accompanied with the change in electronic band structure in the NbN system[36].

Films of NbN were also deposited at a higher temperature. As shown in Figure 2, NbN films of 50 nm thickness grown at 700°C have a lower T_c (almost by 1.2 K) than films grown at 600°C. This is contrary to the expected trend, which predicts an increased fraction of B1 phase, leading to improved superconducting properties with increasing deposition temperature. We believe that this is likely due to oxidation of NbN thin films during cooling
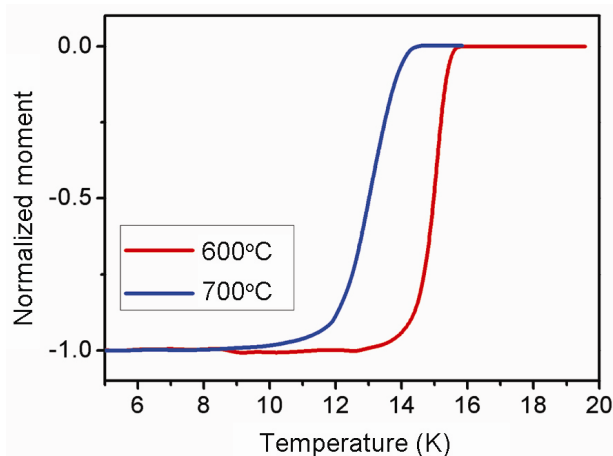
in vacuum, immediately after deposition. Using transmission electron microscopy (TEM) and electron energy loss spectroscopy (EELS) analyses, the formation of an amorphous layer at the filmsubstrate interface due to interdiffusion of Nb, Si, N, O at higher deposition temperatures has been reported previously[35]. However, this was not verified further, as the objective of this study was to synthesize high quality ultrathin superconducting films at lower growth temperature.

Samples were also grown on Si/SiO$_2$ at 200°C substrate temperature with Ar to N_2 ratio of 7:1. A sputtering power of 190 W was used to maintain the growth rate. Thickness of the NbN film was controlled by the deposition time. It is seen from the resistance vs temperature plot of 10 nm thick NbN (Figure 3) that there is no significant degradation of superconductivity in terms of T_c and transition width (ΔT). The best sample in the form of a 50 μm wide strip shows a T_c of about 15.5 K with $\Delta T \approx 1$ K. Drastic reduction in T_c in ultra thin superconducting films, with thickness comparable to the coherence length is expected and can be explained in the framework of intrinsic proximity effect[37]. Based on the numerical calculation proposed by Fominov *et al.*[37], Llin *et al.*[35] estimated a 0.6 nm thick non-superconducting boundary layer at each side of the superconductor which essentially reduces the thickness of the superconducting channel from the measured value.

The process flow for nanofabrication using EBL route is shown in Figure 4. A set of experimental conditions for routinely fabricating high-resolution nanostructures has been developed after several test runs. 10 nm thick NbN films on Si/SiO$_2$ were used. The 10 μm × 10 μm pattern area consists of a meander structure with 100 nm-wide wires and 50% filling factor. EBL was performed in Raith e-line lithography system. The SEM image of the pattern area is shown in Figure 5. The images confirm the
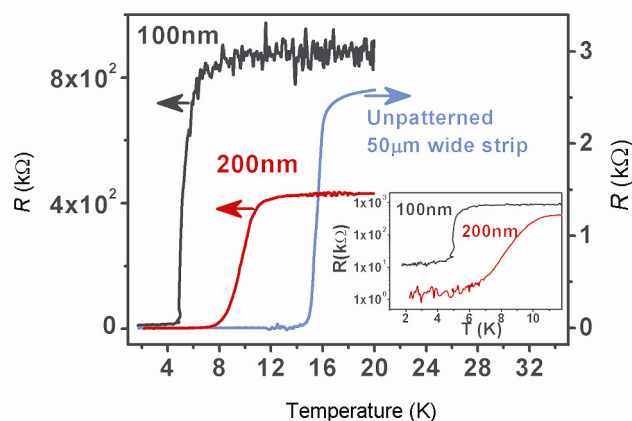

Figure 2. Normalized magnetic moment versus temperature plots for 50 nm thick NbN films grown at 600°C and 700°C. Magnetization measurements were performed at an applied field of 100 G. Prior to the measurements, samples were first cooled under zero-field condition down to the lowest temperature.

Figure 3. Resistance versus temperature plots of as-deposited NbN microstrip and NbN nanowires fabricated using FIB technique. FIB milled samples show non-zero resistive transition and reduction in superconducting transition temperature. Inset zooms in the low temperature behaviour of nanowires.
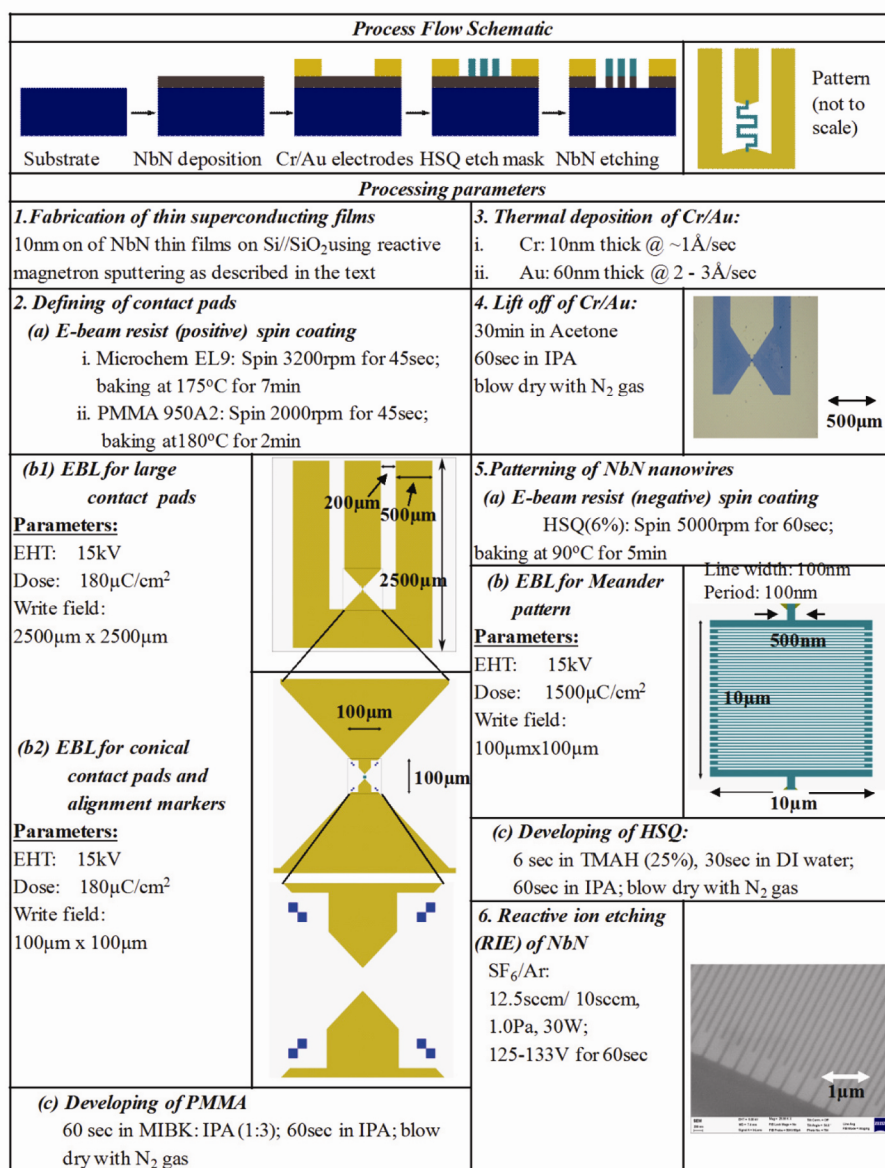
Figure 4. Fabrication process of NbN nanowires using electron beam lithography and reactive ion etching.

optimization of process parameters for precise and accurate transfer of patterns with desired dimensions.

Figure 6 shows the comparison between the superconducting transitions of the unpatterned area of the sample and a patterned meander. In principle, the resistance of the patterned area should increase by two to three orders of magnitude after patterning. However, we do not see any change in resistance. Incomplete removal of NbN from the uncovered portion of the pattern area during the reactive ion etching process is the likely cause for such discrepancy. However, it is important to note that the temperature corresponding to zero resistance and the superconducting transition width are the same in both cases, which confirms that processes involved in EBL do not alter the superconducting properties.

FIB milling was performed in a Auriga, Zeiss dual beam system with an accelerating voltage of 30 kV. Micro strip (50 μm-wide NbN) in four-probe measurement configuration was deposited using shadow mask. In order to avoid edge non-uniformity, a specially designed bi-level mask made out of 75 μm thick, hard electroformed nickel plate with ultra sharp edge profiles was used. NbN micro strips were loaded in the FIB chamber for device fabrication. The narrow junctions of NbN films were at first localized using field emission scanning electron microscope (FESEM). The electron and gallium ion beams were aligned at the same point and utmost care was taken not to expose these junctions to gallium ion imaging. Elemental analysis was carried out using energy dispersive spectroscopy (EDS) measurements. EDS plot
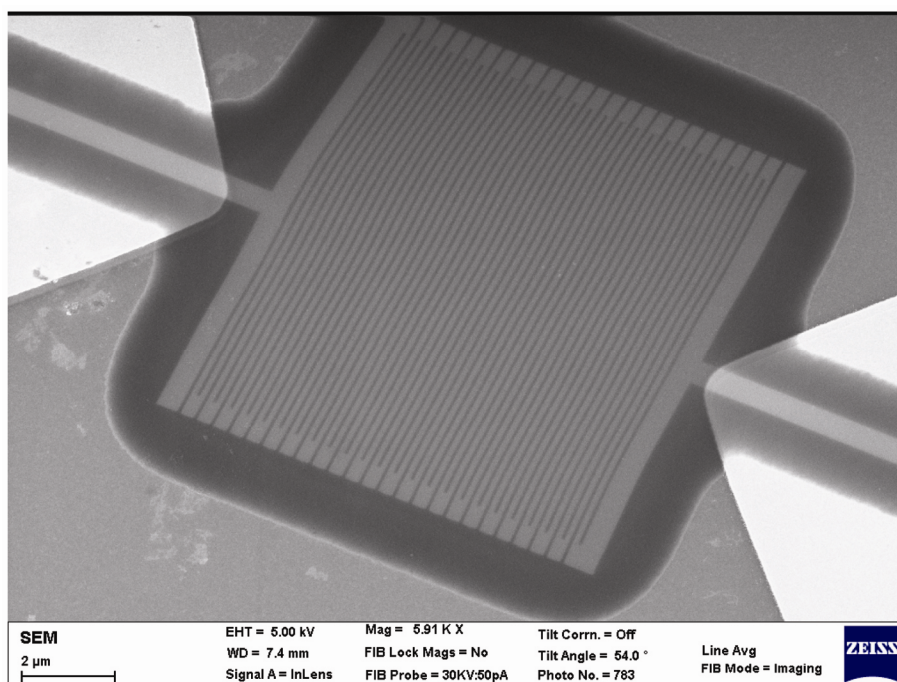
Figure 5. Scanning electron microscopy image of meander patterning over 10 μm × 10 μm area using EBL and RIE. 100 nm wide NbN meander line without any discontinuity is connected to the conical shaped Cr/Au contact pads on both sides of the pattern area. The other ends of the pads are connected to the bigger Cr/Au pads (not shown in the figure) for providing access to wire bonding for transport measurements.
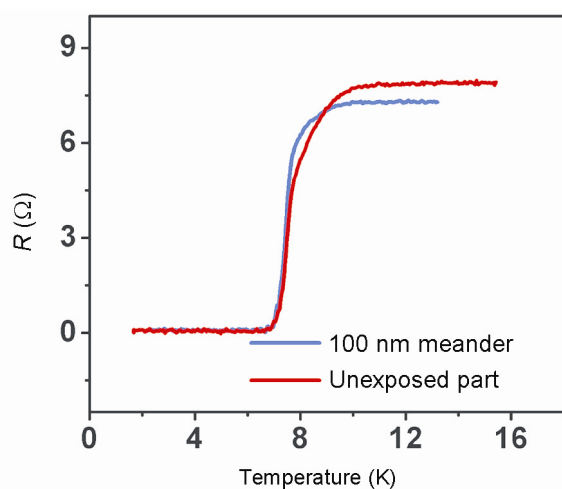

Figure 6. Comparison of resistance versus temperature plot of nanowires fabricated using EBL and RIE with 10 nm thick pristine NbN thin films. The plot presents data while the sample was cooling down from the normal state. Measurements were carried out both during heating and cooling cycles with a temperature sweeping rate of 0.5 K/min. The identical temperature dependence of resistance for both heating and cooling cycles ensures absence of any thermal lag.

in the inset of Figure 7 a confirms that NbN was removed completely from the exposed area, and there was significant amount of gallium implantation during milling. EDS measurements from the remaining portion of NbN which was not exposed to the gallium ion imaging or milling did not show any sign of gallium deposition (Figure 7 b). The

milling pattern of meander lines was optimized and the same milling parameters and conditions were used to obtain the required pattern at very low ion beam current ~50 pA (Figure 7 c). The sample then underwent a second lithography step, in which the narrow junction strip of NbN was further milled at higher ion beam current ~240 pA (Figure 7 d) to remove extra NbN from the edges of the pattern area, thereby ensuring the presence of only meander line connection between the contact pads for the transport measurements.

The resistive transition of FIB patterned nanostructures was compared with the unpatterned 50 μm NbN strip in Figure 3. The measurements were carried out on meander patterns with 100 nm and 200 nm line width and 50% filling factor over 10 μm × 20 μm area. Micro strip and as nano patterns were made on the same chip to avoid run to run variation in superconducting properties. T_c decreased upon nanopatterning due to gallium ion exposure and decreased further as the width of nanowires was reduced to 100 nm. It is important to note here the presence of residual resistance in $R(T)$ curves even at $T = 2$ K. Influence of gallium implantation during focused ion beam milling on superconductivity of niobium micro strip was studied by Datesman et al.[28]. Although a trend of decreasing T_c and increasing onset resistance with increasing gallium dose was observed, all samples however showed complete superconducting transition. The residual resistance after ion milling was observed by Litombe et al. on high T_c-cuprates[38]. Refinement of lithographic processes resulted
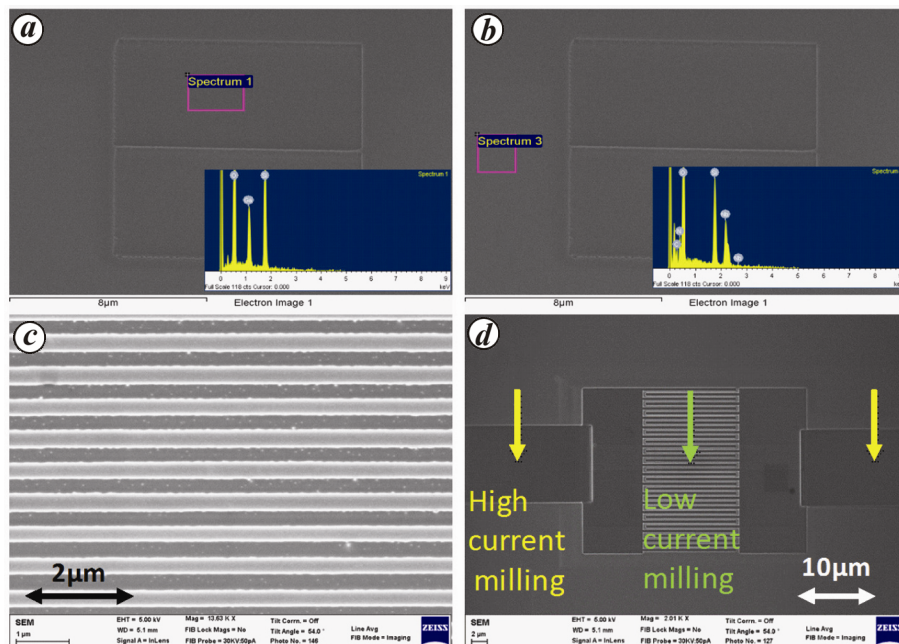
Figure 7 *a–d*. Fabrication of superconducting meander lines of 200 nm line width using focused ion beam (FIB) technique. EDS measurements were carried out on both exposed and unexposed beam area of samples and marked with magenta coloured box in *a* and *b*. As shown in the insets, EDS measurements confirm the presence of gallium implantation only at the exposed area of the samples. *c* shows uniformity of meander pattern within 10% variation in line width. *d* shows the complete patterned (10 μm × 20 μm) area with extended NbN arms on both sides for deposition of Cr/Au contact pads. Left and right arrows indicate the patterned area using high beam current and the centre arrow indicates the pattern area composed of meander lines milled with low beam current.

in complete superconducting transitions in nanowires, down to 80 nm wide and 20 nm thick optimally doped $La_{2-x}Sr_xCuO_4$ films.

We believe that the residual resistance in our case is due to nucleation of gallium ion-mediated non-superconducting regime along the cross-section of the nanowires at certain places. Lateral gallium contamination due to highly focused ion beam in silicon in the vicinity of the processed area was observed earlier[29]. The cause of lateral implantation is believed to be due to redepostion of sputtered gallium ions. Mayer *et al.*[30] also reported the formation of an amorphous layer in a sidewall of silicon due to gallium ions. With FIB milling using gallium ion they observed that the damage in the side wall can extend up to 22 nm in silicon. Mayer *et al.*[30] argued that the result of gallium implantation may range from complete amorphization, as in the case of semiconductor materials, to the formation of defect agglomerates and even inter-metallic phases, in the case of certain metals.

The meander pattern used in this study has 50% filling factor and the patterned area is the same in both cases. Therefore, reducing the width of the nanowire by a factor of half, essentially doubles the length of the wire while decreasing the cross-section by a factor of half. Assuming simple ohmic behaviour, this in turn estimates that the residual sheet resistance of the pattern with 100 nm wide line is higher by a factor of five of patterns with 200 nm wide line. However, our measurement shows that the

residual resistance increased almost by an order of magnitude (from ~1 kΩ to 10 kΩ) with decrease in the width of the line. This discrepancy can be understood qualitatively if we assume that the residual resistance observed in our samples is due to gallium ion implantation which is directly proportional to the dose of implanted gallium ion. As the ion beam exposure time for the pattern with 100 nm wide line is two times larger than that for the pattern with 200 nm wide line, it is obvious that the residual resistance of the former pattern will be higher than the estimated value.

Voltage versus current (*V–I*) characteristics of micro strip and nanopatterns are shown in Figure 8. The *V–I* curve of the micro strip shown (Figure 8 *a*) is hysteretic and shows a sharp jump from superconducting to normal state. The critical current (I_c) at which this jump takes place is found to be 1.5 mA. On reversing the applied voltage, the strip returns to superconducting state when equilibrium between the Joule heating and energy dissipation into the substrate is achieved. *V–I* for both patterns are non-linear. Although it is not possible to deduce I_c from the measurements owing to incomplete superconducting transition, qualitatively we can argue from the shape of the curve that I_c must be low when compared to I_c of devices with similar dimensions. Figure 8 *b* also compares the *V–I* curve of 200 nm wide line pattern measured at two different temperatures (2 K and 5 K). The shape of the nonlinear *V–I* plot measured at 5 K is
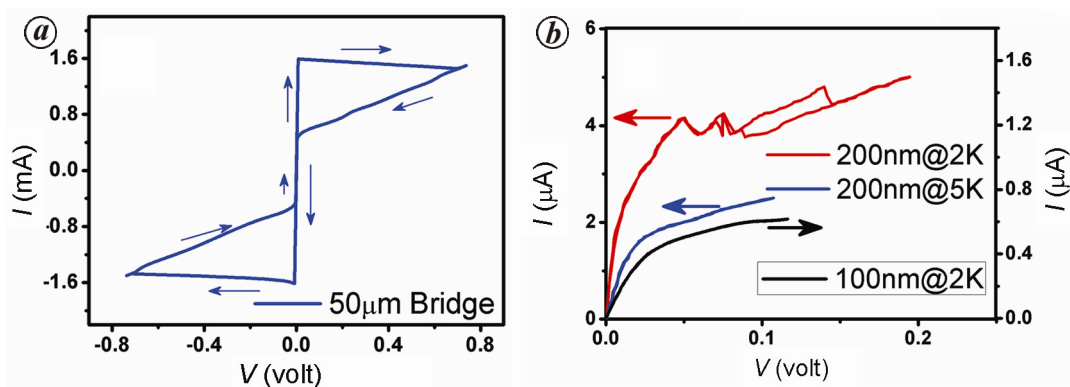
Figure 8. Current–voltage characteristics of NbN. *a* shows *V–I* data of as-deposited NbN micro strips. *b* compares *V–I* measurements of 100 and 200 nm wide meander lines fabricated using FIB milling. The nonlinear and non-hysteretic behaviour evolves into a step-like behaviour particularly at higher bias voltage when measurement temperature decreases from 5 K to 2 K for 200 nm wide line meanders.

similar to 2 K data for 100 nm wide line pattern, and does not have any hysteretic nature. *V–I* curve for patterns with 200 nm wide line measured at 2 K, in particular is however interesting. It shows some hysteretic behaviour at higher currents. The step-like behaviour, although not prominent, is typically associated with phase slip process. Incomplete superconducting resistive transitions and the steps in *V–I* have been reported previously[39,40]. Dissipation and/or fluctuations due to generation of phase slip centres in the case of one-dimensional superconducting structures or vortex antivortex pair generation in two-dimensional systems leads to destruction of long range superconducting order parameter. Although the nano-wires in our case are much wider than the coherence length (typically 4–5 nm in NbN), the presence of local constrictions and/or inhomogeneities associated with FIB milling as mentioned previously cannot be ruled out.

Conclusion

Ultrathin films of NbN were deposited on crystalline MgO as well as on amorphous (Si/SiO$_2$) substrates. The optimization of NbN thin film fabrication for high T_c was performed. The effects of deposition conditions, particularly the ratio of Ar/N$_2$, were studied in an effort to optimize superconducting properties in NbN. It was found that there was no significant decrease in T_c on reducing the thickness of films from 50 nm to 10 nm. Nano structures were fabricated on 10 nm thick NbN films using EBL as well as FIB techniques. EDS measurements confirm gallium implantation in FIB based nano patterns. Although EBL route was found to be a better choice when it came to superconducting nanostructuring, considering the simplicity of FIB milling, efforts are currently being directed towards understanding the effect of gallium contamination on superconducting properties. In order to prevent degradation of superconducting properties due to gallium implantation, research initiatives on capping layer which not only protects the underneath superconducting layer, but also influences the device performance have a lot of potential in applications in single photon technologies.

1. Gol'tsman, G. N. *et al.*, Picosecond superconducting single-photon optical detector. *Appl. Phys. Lett.*, 2001, **79**, 705–707.
2. Takesue, H., Nam, S. W., Zhang, Q., Hadfield, R. H., Honjo, T., Tamaki, K. and Yamamoto, Y., Quantum key distribution over a 40-dB channel loss using superconducting single-photon detectors. *Nat. Photon.*, 2007, **1**, 343–348.
3. Hadfield, R. H., Single-photon detectors for optical quantum information applications. *Nat. Photon.*, 2009, **3**, 696–705 and references therein.
4. Rosenberg, D. *et al.*, Practical long-distance quantum key distribution system using decoy levels. *New J. Phys.*, 2009, **11**, 045009(1–10).
5. Stucki, D. *et al.*, High rate, long-distance quantum key distribution over 250 km of ultra low loss fibres. *New J. Phys.*, 2009, **11**, 075003(1–9).
6. Liu, Y. *et al.*, Decoy-state quantum key distribution with polarized photons over 200 km. *Opt. Express*, 2010, **18**, 8587–8594.
7. Eisaman, M. D., Fan, J., Migdal, A. and Polyakov, S. V., Invited review article: single-photon sources and detectors. *Rev. Sci. Instrum.*, 2011, **82**, 071101(1–25) and references therein.
8. Natarajan, C. M., Tanner, M. G. and Hadfield, R. H., Superconducting nanowire single-photon detectors: physics and applications. *Supercond. Sci. Tech.*, 2012, **25**, 063001(1–16) and references therein.
9. Wang, S. *et al.*, 2 GHz clock quantum key distribution over 260 km of standard telecom fiber. *Opt. Lett.*, 2012, **37**, 1008–1010.
10. Yao, X.-C. *et al.*, Experimental demonstration of topological error correction. *Nature*, 2012, **482**, 489–494.
11. Ma, X.-S. *et al.*, Quantum teleportation over 143 kilometres using active feed-forward. *Nature*, 2012, **489**, 269–273.
12. Pan, J.-W., Chen, Z.-B., Lu, C.-Y., Weinfurter, H., Zeilinger, A. and Żukowski, M., Multiphoton entanglement and interferometry. *Rev. Mod. Phys.*, 2012, **84**, 777–838.
13. Shimizu, K. *et al.*, Performance of long-distance quantum key distribution over 90-km optical links installed in a field environment of Tokyo metropolitan area. *J. Lightwave Technol.*, 2014, **32**, 141–151.

14. Northup, T. E. and Blatt, R., Quantum information transfer using photons. *Nat. Photon.*, 2014, **8**, 356–363.

15. Korzh, B. *et al.*, Provably secure and practical quantum key distribution over 307 km of optical fibre. *Nat. Photon.*, 2014, **9**, 163–168.

16. Takesue, H., Dyer, S. D., Stevens, M. J., Verma, V., Mirin, R. P. and Nam, S. W., Quantum teleportation over 100 km of fiber using highly efficient superconducting nanowire single-photon detectors. *Optica*, 2015, **2**, 832–835.

17. Engel, A., Renema, J. J., Il'in, K. and Semenov, A., Detection mechanism of superconducting nanowire single-photon detectors. *Supercond. Sci. Tech.*, 2015, **28**, 114003(1–22) and references therein.

18. Chunnilall, C. J., Degiovanni, I. P., Kück, S., Müller, I. and Sinclair, A. G., Metrology of single-photon sources and detectors: a review. *Opt. Eng.*, 2014, **53**, 081910(1–17).

19. Lita, A. E., Miller, A. J. and Nam, S. W., Counting near-infrared single-photons with 95% efficiency. *Opt. Express*, 2008, **16**, 3032–3040.

20. Miki, S. *et al.*, Large sensitive-area NbN nanowire superconducting single-photon detectors fabricated on single-crystal MgO substrates. *Appl. Phys. Lett.*, 2008, **92**, 061116(1–3).

21. Korneev, A. *et al.*, Recent nanowire superconducting single-photon detector optimization for practical applications. *IEEE Trans. Appl. Supercond.*, 2013, **23**, 2201204(1–4).

22. Bergeal, N., Grison, X., Lesueur, J., Faini, G., Aprili, M. and Contour, J.-P., High T_c superconducting quantum interference devices made by ion irradiation. *Appl. Phys. Lett.*, 2006, **89**, 112515(1–3).

23. Delacour, C. *et al.*, Superconducting single photon detectors made by local oxidation with an atomic force microscope. *Appl. Phys. Lett.*, 2007, **90**, 191116(1–3).

24. Lee, S.-G., Oh, S., Kang, C. S. and Kim, S.-J., Superconducting nanobridge made from $YBa_2Cu_3O_7$ film by using focused ion beam. *Phys. C Supercond.*, 2007, **460**, 1468–1469.

25. Curtz, N., Koller, E., Zbinden, H., Decroux, M., Antognazza, L., Fischer, Ø. and Gisin, N., Patterning of ultrathin YBCO nanowires using a new focused-ion-beam process. *Supercond. Sci. Technol.* 2010, **23**, 045015(1–6).

26. Zhang, C. *et al.*, Fabrication of superconducting nanowires from ultrathin MgB_2 films via focused ion beam milling. *AIP Adv.*, 2015, **5**, 027139(1–8).

27. Bachar, G., Baskin, I., Shtempluck, O. and Buks, E., Superconducting nanowire single photon detectors on-fiber. *Appl. Phys. Lett.*, 2012, **101**, 262601(1–3).

28. Datesman, A. M., Schultz, J. C., Cecil, T. W., Lyons, C. M. and Lichtenberger, A. W., Gallium ion implantation into niobium thin films using a focused-ion beam. *IEEE Trans. Appl. Supercond.*, 2005, **15**, 3524–3527.

29. Lehrer, C., Frey, L., Petersen, S., Mizutani, M., Takai, M. and Ryssel, H., Defects and gallium-contamination during focused ion beam micro machining. In Proceedings of IEEE Ion Implantation Technology, 2000, pp. 695–698.

30. Mayer, J., Giannuzzi, L. A., Kamino, T. and Michael, J., TEM sample preparation and FIB induced damage. *MRS Bull.*, 2007, **32**, 400–407.

31. Venkataraj, S., Drese, R., Liesch, Ch., Kappertz, O., Jayavel, R. and Wuttig, M., Temperature stability of sputtered niobium-oxide films. *J. Appl. Phys.* 2002, **91**, 4863–4871.

32. Ziegler, M., Fritzsch, L., Day, J., Linzen, S., Anders, S., Toussaint, J. and Meyer, H.-G., Superconducting niobium nitride thin films deposited by metal organic plasma-enhanced atomic layer deposition. *Supercond. Sci. Technol.*, 2013, **26**, 025008(1–5).

33. Thakoor, S., Lamb, J. L., Thakoor, A. P. and Khanna, S. K., High T_c superconducting NbN films deposited at room temperature. *J. Appl. Phys.*, 1985, **58**, 4643–4648.

34. Wang, Z., Kawakami, A., Uzawa, Y. and Komiyamaa, B., Superconducting properties and crystal structures of single-crystal niobium nitride thin films deposited at ambient substrate temperature. *J. Appl. Phys.*, 1996, **79**, 7837–7842.

35. Ilin, K. *et al.*, Ultra-thin NbN films on Si: crystalline and superconducting properties. *J. Phys.: Conf. Ser.*, 2008, **97**, 012045(1–6).

36. Chockalingam, S. P., Chand, M., Jesudasan, J., Tripathi, V. and Raychaudhuri, P., Superconducting properties and Hall effect of epitaxial NbN thin films. *Phys. Rev. B Condens. Matter*, 2008, **77**, 214503(1–8).

37. Fominov, Y. V. and Feigel'man, M. V., Superconductive properties of thin dirty superconductor–normal-metal bilayers. *Phys. Rev. B Condens. Matter*, 2001, **63**, 094518(1–14).

38. Litombe, N. E., Bollinger, A. T., Hoffman, J. E. and Božovic, I., $La_{2-x}Sr_xCuO_4$ superconductor nanowire devices. *Phys. C Supercond.*, 2014, **506**, 169–173.

39. Elmurodov, A. K. *et al.*, Phase-slip phenomena in NbN superconducting nanowires with leads. *Phys. Rev. B Condens. Matter*, 2008, **78**, 214519(1–5).

40. Delacour, C., Pannetier, B., Villegier, J.-C. and Bouchiat, V., Quantum and thermal phase slips in superconducting niobium nitride (NbN) ultrathin crystalline nanowire: application to single photon detection. *Nano Lett.*, 2012, **12**, 3501–3506.